Petroleum Science 23 (2026) 868–881

Contents lists available at ScienceDirect

Petroleum Science

journal homepage: www.keaipublishing.com/en/journals/petroleum-science

Original Paper

NMR-monitored CH_4 adsorption/desorption dynamics in shale: Implications for CO_2-ESGR and in-situ sequestration

Sheng-Ming Huang [a,b], Guan-Cheng Jiang [a,*], Jun Yang [a], Chun-Ping Guo [a], Quan-De Wang [a], Teng-Fei Dong [c], Yin-Bo He [a], Li-Li Yang [a], Qing-Gong Liu [d], Zhe-Hui Jin [b,**]

[a] College of Petroleum Engineering, Ministry of Education (MOE) Key Laboratory of Petroleum Engineering, China University of Petroleum (Beijing), Beijing, 102249, China
[b] School of Mining and Petroleum Engineering, Department of Civil and Environmental Engineering, University of Alberta, Edmonton, T6G 1H9, Canada
[c] College of Science, China University of Petroleum (Beijing), Beijing, 102249, China
[d] Ningxia Geek Space Construction Technology Co., Ltd., Yinchuan, 750002, Ningxia, China

ARTICLE INFO

Article history:
Received 20 May 2025
Received in revised form
30 October 2025
Accepted 2 November 2025
Available online 6 November 2025

Edited by Yan-Hua Sun

Keywords:
Multi-phase CH_4 desorption
Competitive adsorption
Nuclear magnetic resonance (NMR)
CO_2-enhanced shale gas recovery (CO_2-ESGR)
Carbon sequestration

ABSTRACT

Addressing the inherent challenges of low recovery rates and difficulties in shale gas extraction, this study investigates the application potential of CO_2-enhanced shale gas recovery (CO_2-ESGR) coupled with carbon sequestration (CS). Utilizing low-field nuclear magnetic resonance (NMR) technology, we conducted real-time monitoring of methane adsorption and desorption processes within collected shale samples. Through the analysis of T_2 spectra and corresponding peak areas, we achieved quantitative differentiation among adsorbed CH_4, free CH_4 within pore spaces, and free CH_4 within fractures. The results demonstrate that within a pressure range of 0.01–10 MPa, the total methane volume increased progressively from 79.4 to 177.83 cm^3/g. Following CO_2 injection, a significant weakening of the short-T_2 signal (representing adsorbed CH_4) was observed, accompanied by a concomitant enhancement of the long-T_2 signal (representing free-phase CH_4). Furthermore, depressurization desorption experiments revealed that CO_2 injection increased the methane desorption rate by approximately 10%, while simultaneously facilitating the long-term, stable sequestration of CO_2 within the shale matrix. These findings not only validate the mechanism of competitive adsorption, whereby CO_2 enhances shale gas recovery, but also highlight the significant carbon sequestration potential of shale reservoirs. Consequently, this research provides a crucial theoretical basis and technical support for advancing both shale gas development and carbon emission reduction strategies.

1. Introduction

As the global shift toward cleaner energy intensifies, shale gas has become a strategic component of national energy portfolios (Cooper et al., 2018; Jiang et al., 2022; Kerr, 2010; Rivard et al., 2014; Wang and Li, 2017; Wang et al., 2014; Yuan et al., 2015; Zou et al., 2015). In 2022, U.S. shale reservoirs produced approximately 8.11×10^{11} m^3 of dry natural gas—about 79% of the nation's total—with projections reaching 9.63×10^{11} m^3 by 2050 (Zeraibi and Khan, 2024). China also holds vast shale reserves, notably 1.2×10^{12} m^3 in the Sichuan Basin (Feng Z. et al., 2022; Sun et al., 2021; Sun et al., 2023; Zhang et al., 2022). However, compared with conventional oil and gas reservoirs, shale formations are characterized by low porosity, low permeability, high water saturation, and a complex multi-scale pore structure, which has kept the recovery efficiency of shale gas at a persistently low level (Feng D. et al., 2022; Huang et al., 2024; Omari et al., 2022; Zhang et al., 2021). Meanwhile, shale gas development faces two critical challenges (Li et al., 2016; Lutz et al., 2013; Yuan et al., 2015). First, due to the high proportion of adsorbed methane in nanopores (40%–60%), the average recovery factor achievable with

* Corresponding author.
** Corresponding author.
E-mail addresses: m15600263100_1@163.com (G.-C. Jiang), zhehui2@ualberta.ca (Z.-H. Jin).
Peer review under the responsibility of China University of Petroleum (Beijing).

https://doi.org/10.1016/j.petsci.2025.11.003

current technologies is only 15%–25%, far below the level of more than 50% typically obtained in conventional gas fields. Second, traditional extraction methods such as hydraulic fracturing pose increasingly severe environmental concerns, including water scarcity, groundwater contamination, and fugitive methane emissions. Studies have shown (Skytt et al., 2020) that the global warming potential of methane is 84 times greater than that of carbon dioxide, which highlights the urgent need for greener approaches to shale gas development.

Understanding methane's occurrence states and transport mechanisms in shale is key to improving extraction efficiency (Feng et al., 2020; Ma et al., 2018). Unlike conventional reservoirs, methane in shale exists as adsorbed, free, or dissolved gas (Chen et al., 2019). Adsorbed methane—bound to organic matter or pore walls and modeled by the Langmuir isotherm—is particularly difficult to recover due to strong fluid–surface interactions (Hu et al., 2023; Tang et al., 2017; Yuan et al., 2014). Traditional studies have primarily focused on isothermal adsorption experiments, low-temperature gas adsorption (e.g., N_2, CO_2), displacement tests, and pressure-depletion desorption experiments, or have relied on numerical and molecular simulations to elucidate the adsorption mechanisms (Huang et al., 2025; Liu L. et al., 2015; Merey, 2019; Qin et al., 2023; Xu H. et al., 2024; Zhang et al., 2020). Despite the significant progress achieved, existing approaches still suffer from several limitations (Bai et al., 2021; Guo, 2013; Liu S. et al., 2015). For example, isothermal adsorption experiments are typically conducted on powdered samples or small rock fragments, which may alter the original pore structure and wettability. Moreover, such tests are mostly static measurements, making it difficult to fully capture the dynamic adsorption/desorption processes within complex pore networks under realistic reservoir conditions. Molecular simulations, constrained by computational resources and model simplifications, struggle to reproduce the inherent complexity and heterogeneity of real shale formations. Conventional displacement experiments often rely on macroscopic inlet–outlet parameters (e.g., pressure, flow rate, and composition), which fail to provide direct insights into the dynamic distribution and phase transitions of fluids within the rock matrix. In particular, accurately, in situ, and in real time monitoring and distinguishing the dynamic migration and transformation of methane across different pore scales—especially under varying gas compositions such as during CO_2 injection—remains a major challenge.

Nuclear magnetic resonance (NMR) has emerged as a powerful, non-destructive tool for investigating shale gas behavior, enabling real-time, phase-specific monitoring of hydrogen nuclear relaxation signals from reservoir fluids (Kausik et al., 2016; Li et al., 2024; Lu et al., 2022; Yang et al., 2022). Widely used in petroleum exploration, NMR supports pore structure characterization, fluid quantification, and permeability estimation. Recent advances in low-field NMR technology and data analysis have expanded its application in unconventional reservoirs, particularly shale formations (Zhao and Wang, 2019; Zhou et al., 2021). By analyzing transverse relaxation time (T_2) distributions, NMR can distinguish adsorbed, confined, and free methane, allowing for dynamic, quantitative tracking of methane during processes such as saturation, desorption, and competitive adsorption (Lu et al., 2023). Compared to conventional techniques, NMR offers real-time, non-invasive monitoring without altering pore structure (Huang and Zhao, 2017; Zhang et al., 2024). However, most current studies focus on isolated adsorption or desorption events, with limited integration of NMR into dynamic processes like CO_2-enhanced shale gas recovery (CO_2-ESGR). To address low shale gas recovery and contribute to greenhouse gas mitigation, CO_2-enhanced shale gas recovery (CO_2-ESGR) has emerged as a promising dual-purpose strategy (Ahn et al., 2020; Liu et al., 2017; Ma et al., 2022; Mohagheghian et al., 2019; Sun et al., 2013). This approach exploits CO_2's stronger adsorption affinity—due to its higher polarizability, quadrupole moment, and smaller kinetic diameter—allowing it to displace adsorbed CH_4 from shale surfaces and enhance methane recovery (Brochard et al., 2012; Huang et al., 2018). Simultaneously, the injected CO_2 can be securely sequestered within the low-permeability shale matrix (Liao et al., 2023; Liu et al., 2019; Sun et al., 2022). Ding et al. (2022) experimentally examined competitive CO_2/CH_4 adsorption in tight gas reservoirs and demonstrated that CO_2 exhibits a higher adsorption capacity. At 24 MPa, over 30% of the initially adsorbed CH_4 was displaced by injected CO_2. Similarly, Tang et al. (2023) used numerical simulations to evaluate the feasibility of CO_2 sequestration coupled with enhanced gas recovery (CO_2-EGR). Their results showed that 45%–60% of the injected CO_2 could be sequestered, while natural gas production increased by 10%–15%, highlighting both economic and environmental advantages. Yuan et al. (2023) employed GCMC and MD simulations to investigate the effects of kerogen maturity and water content on the adsorption and diffusion of CH_4 and CO_2. The results demonstrated that higher kerogen maturity leads to greater porosity and connectivity, thereby enhancing gas adsorption and diffusion, with CO_2 showing a pronounced adsorption advantage and stronger selectivity. Increasing water content reduces the adsorption and diffusion capacities of both gases, with CO_2 being more significantly affected; however, the relative selectivity of CO_2 over CH_4 is improved, which favors CO_2 displacement of CH_4. Overall, kerogen maturity and water content are identified as key controlling factors, and highly mature kerogen exhibits greater potential for CO_2 sequestration and enhanced gas recovery (CS-EGR). Despite such promising findings, a systematic, dynamic understanding of the pore-scale kinetics and microscopic responses during CO_2/CH_4 competitive adsorption remains insufficiently explored.

This study investigates samples from the Qiongzhusi Formation in the Sichuan Basin, China, applying low-field NMR technology throughout the full CO_2-ESGR process. This approach enables detailed, quantitative tracking of CH_4 adsorption and dynamic desorption behavior under simulated reservoir conditions, particularly during CO_2 injection. The primary objectives are to uncover the microscopic mechanisms governing CO_2-driven methane displacement and evaluate the potential for simultaneous carbon sequestration within the shale matrix. The research follows a multi-stage methodology: (1) Dynamic CH_4 adsorption/desorption experiments are conducted across a pressure range of 0.01–10 MPa to obtain T_2 spectra and determine methane distribution across adsorbed and free phases. (2) After CH_4 adsorption equilibrium is reached, CO_2 is injected, and the evolution of T_2 spectra is continuously monitored to capture the real-time behavior of the CO_2–CH_4 competitive adsorption process. (3) Comparative depressurization desorption experiments are then performed to quantify the difference in methane release efficiency with and without CO_2 injection. Gas chromatography (GC) analysis further validates CO_2 sequestration performance. This study aims to establish a robust quantitative relationship between methane volume and T_2 signal intensity, providing a novel methodology for real-time monitoring of fluid dynamics during CO_2-ESGR. The findings are expected to support optimization of field-scale injection strategies and demonstrate the dual benefits of enhanced gas recovery and CO_2 geological storage.

2. Experimental section

2.1. Samples

For this study, shale samples were obtained from the Qiongzhusi Formation in the Sichuan Basin, China, at depths ranging from 3044 to 3233 m, as shown in Fig. 1. The Sichuan Basin is one of China's most shale gas-rich regions, with Lower Paleozoic source rocks characterized by widespread distribution, considerable thickness, high thermal maturity, abundant microfractures, and strong hydrocarbon generation potential. Table 1 summarizes the physical properties of two representative samples used in this research. The Qiongzhusi shale is known for its well-developed organic matter porosity. The average porosity of the tested samples is 3.49%, and the average total organic carbon (TOC) content is 1.71%, indicating moderate to good organic richness. Mineralogical analysis reveals that the samples primarily consist of quartz and clay minerals, with minor amounts of plagioclase and pyrite. The relatively high content of brittle minerals is favorable for both shale gas formation and accumulation. High-purity CH_4 and CO_2 gases (99.99%) used in the experiments were supplied by Beijing Xingchen Oxygen Co., Ltd. Prior to testing, all shale samples were oven-dried at 70 °C for 24 h to eliminate residual moisture.

2.2. Experimental setup

The experiments were performed using the NIUMAG MacroMR12-150H-I system (Niumag, China), a specialized platform designed for real-time monitoring and evaluation of fluids in tight reservoirs. This integrated system comprises several core components: a large-aperture NMR analysis module, a gas/fluid injection unit, a high-temperature/high-pressure (HTHP) saturation chamber, an imaging system, and a data acquisition module. A schematic of the experimental setup is shown in Fig. 2. The specific NMR scanning parameters used in this study are listed in Table 2. During testing, confining pressure was precisely controlled by injecting fluorocarbon oil via a syringe pump. This oil was chosen for its hydrogen-free composition, which ensures that it does not interfere with the acquisition or interpretation of NMR T_2 relaxation spectra. All NMR measurements in this study were conducted at laboratory temperature (25 °C) rather than under in situ reservoir conditions. Therefore, although the injection pressure of CO_2 was as high as 15 MPa, its fluid state was unlikely to be supercritical, given that the experimental temperature remained below the critical temperature of 31.1 °C.

Fig. 1. Shale samples from the Qiongzhusi Formation, Sichuan Basin, China.

Principle of NMR measurement (Kleinberg and Vinegar, 1996; Straley et al., 1997): In a low-field magnetic environment, NMR measurements capture the amplitude and decay rate of relaxation signals emitted by hydrogen nuclei within the fluids contained in rock cores. By inverting the measured relaxation signal, a transverse relaxation time (T_2) spectrum can be obtained. Compared to longitudinal relaxation time (T_1) measurements, T_2 analysis is preferred in reservoir fluid evaluation due to its greater time efficiency, ease of implementation, and suitability for fluid phase differentiation. In the context of shale gas, quantitative analysis of methane phases is directly correlated with the number of hydrogen atoms present in methane molecules. During standard T_2 measurements targeting hydrogen nuclei in methane, the resulting T_2 spectrum is affected by three primary relaxation mechanisms: bulk relaxation (T_{2B}), surface relaxation (T_{2S}), and diffusion-induced relaxation (T_{2D}). The overall T_2 relaxation time (T_2) can be described by Eq. (1) (Yao et al., 2019):

$$\frac{1}{T_2}=\frac{1}{T_{2B}}+\frac{1}{T_{2S}}+\frac{1}{T_{2D}}=\frac{3T_k}{298\eta}+\rho_2\left(\frac{S}{V}\right)+\frac{D(\gamma G T_E)^2}{12} \quad (1)$$

where T_{2B}, T_{2S}, and T_{2D} denote the bulk, surface, and diffusion relaxation times, μs, respectively; T_k is the measurement temperature, K; η is the fluid viscosity, Pa·s; ρ_2 is the surface relaxivity, $s^{-1}\cdot\mu m^{-1}$; S is the pore surface area, μm^2; V is the pore volume, μm^3; D is the diffusion coefficient of methane molecules—at 298 K, $D=(1–2)\times10^{-5}$ m^2/s; γ is the gyromagnetic ratio of the hydrogen nucleus (2.68×10^8 $rad\cdot s^{-1}$); G is the magnetic field gradient (0.00027 T/m); and T_E is the echo spacing in the CPMG pulse sequence, ms.

By calculation, the value of $1/T_{2D}$ is $(9.82–19.6)\times10^{-5}$ ms^{-1} (Zheng et al., 2022), hence, the diffusion relaxation in shale porous media can generally be neglected, and Eq. (1) can be simply expressed as Eq. (2):

$$\frac{1}{T_2}=\frac{1}{T_{2B}}+\rho_2\left(\frac{S}{V}\right) \quad (2)$$

Low-field NMR enables dynamic characterization of state transitions and gas-migration features during methane adsorption and desorption in shale by measuring the T_2 relaxation signals of CH_4 hydrogen nuclear. By analyzing the time-dependent changes in the T_2 spectra, the adsorption and desorption mechanisms of shale gas can be revealed in both an intuitive and quantitative manner.

2.3. Experimental procedure

The experimental procedure can be divided into the following parts, including the dynamic adsorption of CH_4, the dynamic desorption of CH_4, and the competitive adsorption of CO_2–CH_4. The experimental steps are as follows (Wen et al., 2022; Yao et al., 2014).

1) CH_4 dynamic adsorption process
   (1) Sample preparation and system leak test: The shale core sample is first dried in an oven at 105 °C for at least 48 h to

Table 1
Physical characteristics of collected shale samples.

Sample ID	Depth, m	TOC, %	Porosity, %	Mineral composition, %						
				Quartz	Potash feldspar	Plagioclase	Calcite	Dolomite	Pyrite	Clay minerals
Q1	3233.17	1.98	3.65	33.3	4.5	11.4	2.1	7.4	7.5	33.8
Q2	3044.70	1.44	3.33	31.0	1.9	9.9	2.7	4.8	6.4	43.3

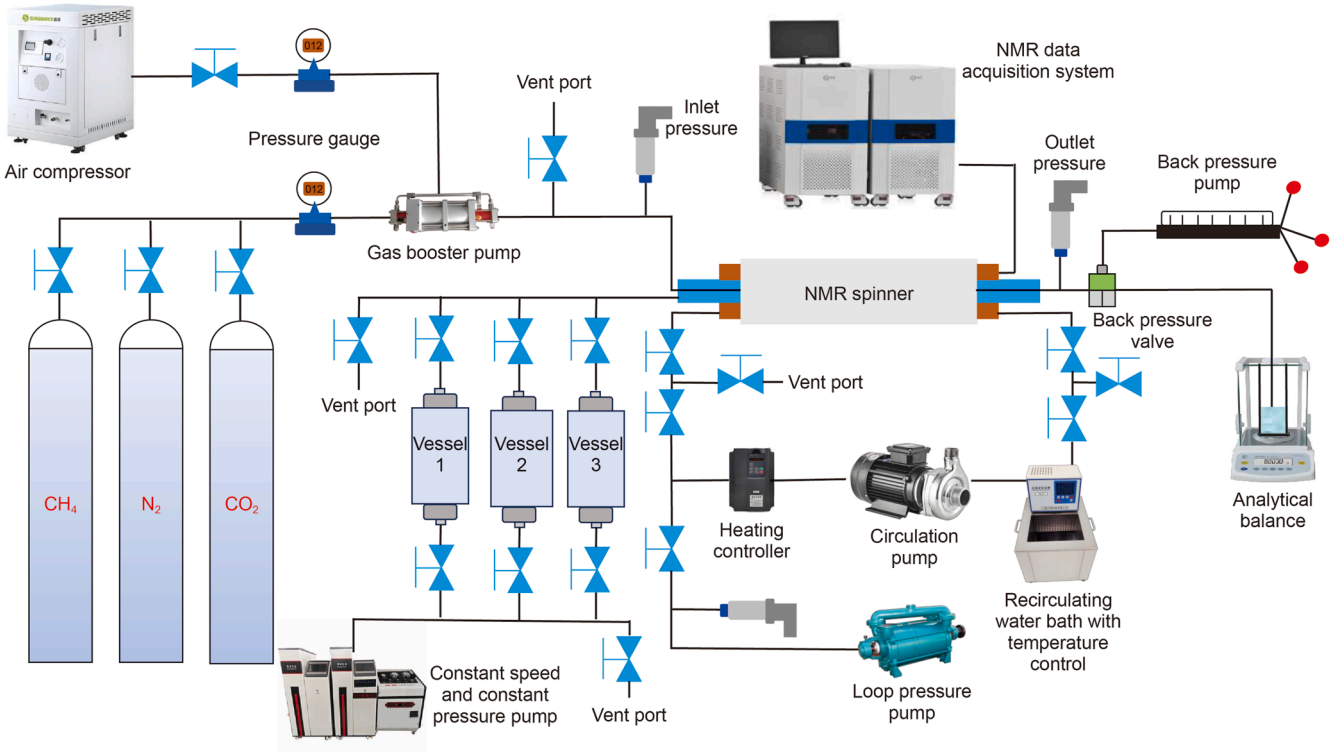

Fig. 2. NMR microstructure and fluid analysis imaging system.

Table 2
NMR instrument scan parameters.

Magnetic field frequency, MHz	Magnetic field strength, T	Waiting time, ms	Minimum echo spacing, ms	Number of echoes	Number of scans
12.448	0.3	3000	0.2	9000	16

eliminate residual moisture. Once dried, the sample is placed into the NMR apparatus. Nitrogen gas is then introduced into the system to conduct a leak test. The system is deemed airtight if no significant pressure fluctuation is observed over a 30-min monitoring period.

(2) System setup and confinement: Following leak validation, the inlet and outlet dead volumes are measured. A confining pressure of 25 MPa is applied to the core sample using an ISCO pump to replicate reservoir stress conditions. Methane (CH_4) is prepared and injected into the core holder housed within the NMR device at controlled pressures.

(3) Pressure stepping and saturation: Methane is introduced incrementally across a pressure range of 0–10 MPa. The pressure is first raised to 2 MPa and held to allow saturation. It is then increased stepwise to 4 MPa, and subsequently up to the maximum of 10 MPa. At each stage, once the target pressure is reached, the inlet valve is closed to isolate the system for equilibrium monitoring.

(4) NMR acquisition and equilibrium monitoring: At each pressure increment, NMR signal acquisition is initiated to track methane saturation within the shale. Equilibrium is considered reached when both the total NMR signal and pressure sensor readings stabilize. T_2 spectra are recorded at fixed intervals (e.g., every 30 min) throughout the saturation period, generating a sequence of T_2 spectra corresponding to each pressure level.

(5) Data analysis and phase differentiation: Using the acquired T_2 signal intensities at various equilibrium pressures, a calibration curve is developed to correlate methane volume with total NMR signal intensity. This relationship enables quantitative analysis of methane distribution among different phases within the shale—specifically distinguishing adsorbed methane, free gas in the pore matrix, and free gas within fractures.

2) Methane dynamic desorption process

Following complete CH_4 saturation of the shale core, a depletion-driven production experiment is conducted via the system's outlet. Initially, the back pressure is reduced to 7 MPa, initiating desorption and production of methane from the core over a defined period. The pressure is then further decreased to 0.1 MPa (near atmospheric), and held constant to allow continued desorption until methane production is deemed largely complete. Throughout the depressurization process, low-field NMR is employed to continuously monitor T_2 spectra, enabling real-time tracking of signal changes associated with different methane phases—specifically adsorbed and free gas—as they are released from the shale. The evolving T_2 data is used to construct recovery profiles, plotting cumulative production or recovery factors for each gas phase over time. These plots are subsequently analyzed to elucidate the production dynamics and phase-specific desorption behavior of methane during pressure depletion.

3) CO_2–CH_4 competitive adsorption process
   The experimental procedure comprises the following key steps:
   (1) Baseline measurement: Prior to gas injection, the initial T_2 spectrum of the dry shale sample is recorded using NMR to establish a reference for subsequent comparisons.
   (2) Methane saturation: CH_4 is injected into the shale sample using a high-pressure pump. During the saturation process, NMR measurements are continuously taken to capture the evolving T_2 spectra and to quantify methane distribution between adsorbed and free phases within the pore network.
   (3) Re-saturation and CO_2 injection: After any desorption experiments are completed, the shale sample is re-saturated with methane following the same procedure as above until dynamic adsorption equilibrium is re-established at 10 MPa. CO_2 is then injected into the methane-saturated sample at a controlled flow rate of 0.05 mL/min using an ISCO pump, with an injection pressure set at 15 MPa.
   (4) Competitive adsorption and monitoring: As CO_2 enters the shale, it competes with CH_4 for adsorption sites, gradually displacing the adsorbed methane. NMR is used in real time to monitor the CH_4 signal intensity, allowing for dynamic tracking of methane displacement and quantification of the changes in gas-phase distribution during CO_2 injection. The process continues until a new adsorption equilibrium is reached.
4) Depletion production process following CO_2–CH_4 competitive adsorption

Once dynamic adsorption equilibrium between CH_4 and CO_2 is established at 15 MPa, the depletion production experiment is initiated. Following a procedure analogous to the earlier methane desorption stage, the back-pressure at the outlet is first reduced to 7 MPa, allowing for the initial release and production of CH_4 and CO_2 from the shale core. After a designated production period, the pressure is further decreased to 0.1 MPa (near-atmospheric) and maintained until gas production becomes negligible, indicating that desorption is substantially complete. Throughout the entire depressurization and production phase, low-field NMR is employed to continuously monitor the evolution of the T_2 spectra. These data are used to analyze the content and phase distribution (i.e., adsorbed vs. free) of the residual CH_4 within the shale sample at various stages of pressure depletion. This dynamic monitoring enables the quantification of methane recovery efficiency and phase-specific production behavior following CO_2 injection, offering valuable insight into the effectiveness of the ESGR process under simulated reservoir conditions.

3. Results and discussion

3.1. Dynamic NMR characteristic analysis of methane adsorption/desorption in shale

3.1.1. CH_4 dynamic adsorption process

Figs. 3 and 4 show the CH_4 T_2 spectra and corresponding peak areas at various saturation pressures. As the shale sample undergoes methane adsorption at increasing pressures, both the NMR T_2 spectra and peak areas change significantly. Fig. 3 illustrates that as the saturation pressure rises from 0.01 to 10 MPa, the methane content in both the short T_2 region (0.01–1 ms) and long T_2 region (> 100 ms) increases. Saturation is largely achieved around 6 MPa. Notably, at higher pressures (e.g., 10 MPa), the short T_2 peak amplitude increases, indicating methane preferentially adsorbing into smaller pores like micropores and nanopores. This enhancement is due to restricted molecular motion in smaller confinements, resulting in faster relaxation and shorter T_2 times. The medium-to-long T_2 range shows more complex behavior, with changes in intensity and possible shifts in peak positions. It is suggested that some of the long T_2 signal represents methane in larger pores or fractures, which may become compressed into smaller pores or adsorbed onto surfaces as pressure increases, causing a decrease in long T_2 intensity or a shift towards longer T_2 times (Sun et al., 2016).

As shown in Fig. 4, as the pressure increases from 0.01 to 10 MPa, the total peak area rises from 253.08 to 504.05, with an overall trend of increasing followed by some fluctuations. The increase in peak area indicates a rise in the detectable methane content within the shale as methane molecules fill the pore system. However, the fluctuations, especially at higher pressures, may occur as adsorption nears saturation or due to pore redistribution effects. At the highest pressures, the total peak area slightly decreases, likely due to accelerated spin-spin (T_2) relaxation in the pore space under high-pressure conditions. The increased molecular confinement at high pressure leads to faster relaxation rates, causing some NMR signals to decay too quickly to be fully detected. Another possible contributing factor is the displacement, movement, or minor leakage of mobile methane components during prolonged high-pressure exposure (Kleinberg et al., 1993).

Based on the total NMR T_2 signal measured at different pressures during the CH_4 adsorption process, a mathematical

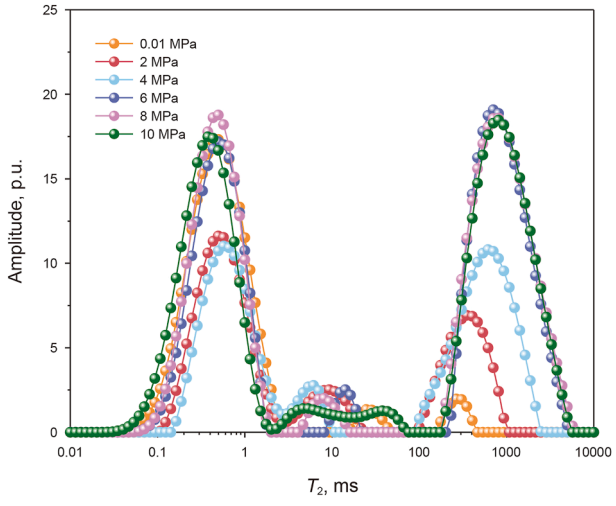

Fig. 3. T_2 spectra of CH_4 at different saturation pressures.

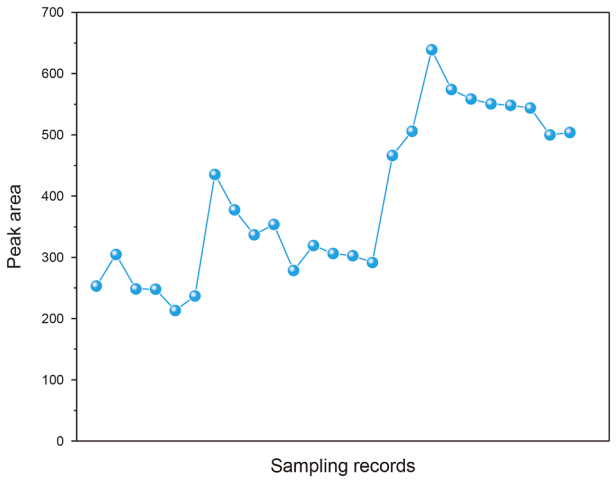

Fig. 4. Peak areas of the CH_4 adsorption process at different sampling intervals.

relationship between the methane intake and the total T_2 signal was established (as shown in Fig. 5). Using this fitted correlation, the volumes of adsorbed CH_4, free CH_4 in pores, and free CH_4 in fractures were derived by partitioning the overall volume according to the integrated areas of the segmented T_2 peaks, with short T_2 corresponding to adsorbed CH_4 and intermediate/long T_2 corresponding to free CH_4.

$$V_{\text{injecting amount}} = 0.593 + 0.3067 \times T_{2\text{signal amplitude}} \quad (3)$$

where $T_{2\text{signal amplitude}}$ represents the total T_2 signal intensity corresponding to CH_4, p.u.; $V_{\text{injecting amount}}$ represents the volume of free-phase CH_4, cm^3.

While the total T_2 signal is correlated with the overall CH_4 volume through Eq. (3), the phase-specific volumes are determined by integrating the peak areas over different T_2 ranges: adsorbed CH_4 (0.01–1 ms), free CH_4 in pores (1–100 ms), and free CH_4 in fractures (> 100 ms). These sub-areas are subsequently scaled using Eq. (3) to obtain quantitative volumes, as illustrated in Figs. 6 and 7. Fig. 6 shows the volumes of adsorbed methane, free-phase methane in pores, and free-phase methane in fractures at various pressures during the saturation process. The volume of adsorbed methane changes gradually, initially decreasing slightly

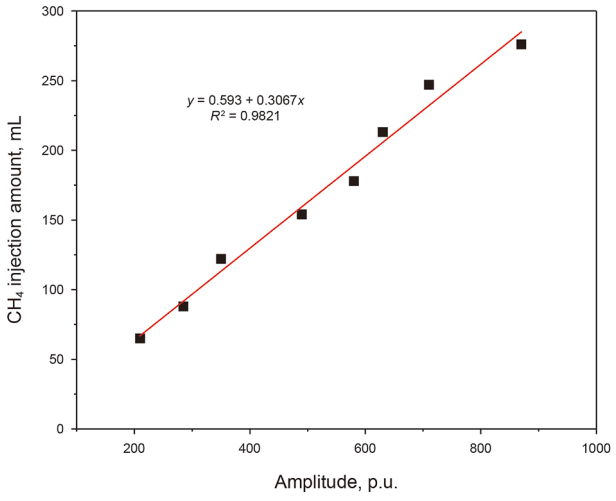

Fig. 5. Linear relationship between NMR signal intensity and CH_4 injection volume.

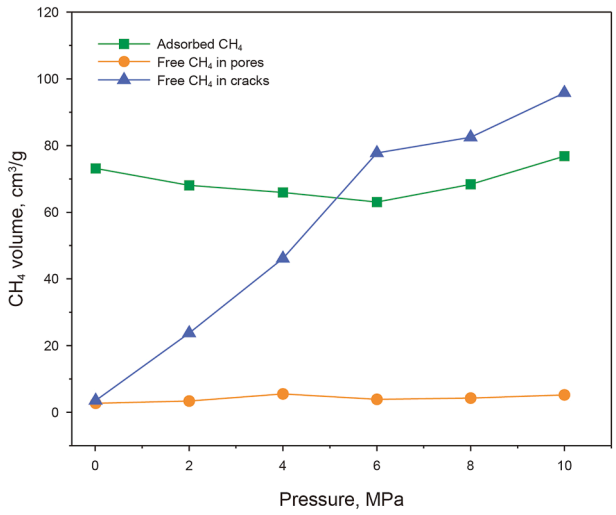

Fig. 6. Pressure dependence of CH_4 in different phases during saturation.

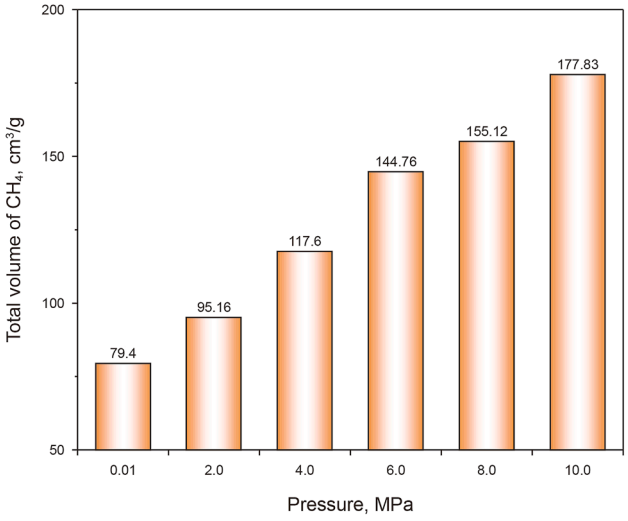

Fig. 7. Variation of total volume of CH_4 adsorbed with pressure during saturation.

from 73.12 cm^3/g at 0 MPa to a minimum of 63.06 cm^3/g at 6 MPa, then rising to 76.78 cm^3/g at 10 MPa. This fluctuation suggests that as the pressure increases, free methane enters the pores and fractures, temporarily occupying adsorption sites and reducing the apparent adsorption capacity. However, at higher pressures, the adsorption density increases, leading to the volume rise. The volume of free-phase methane within pores remains relatively stable, ranging from 0 to 10 cm^3/g, indicating limited storage capacity in the rigid micropores, which are less prone to expansion. In contrast, the volume of free-phase methane within fractures increases sharply with pressure, rising from 3.56 cm^3/g at 0.01 MPa to 95.83 cm^3/g at 10 MPa. This demonstrates that fractures and larger connected pores play a significant role in methane storage, with their capacity for storing free-phase methane highly sensitive to pressure changes.

Fig. 7 shows the variation in the total methane volume within the shale sample during the saturation process at different pressures. As the pressure increases, the total methane volume consistently rises, from 79.4 cm^3/g at 0.01 MPa to 177.83 cm^3/g at 10 MPa. Based on the phase volume analysis in Fig. 6, we found that in the low-pressure range (0.01–4 MPa), although the

adsorbed methane dominates the total volume, the increase in overall storage is primarily attributed to the rapid filling of microfracture networks by free methane (Zheng et al., 2021). In this stage, both adsorption and free-gas compression occur with increasing pressure, but the incremental volume is mainly contributed by the latter. In the medium to high-pressure range (> 4 MPa), the continued volume increase is mainly driven by the expansion of the fracture network, with free-phase methane becoming the dominant component. At this stage, the fracture system becomes the primary storage space for shale gas, with free methane dominating. In the subsequent stage, CO_2 can be utilized to displace adsorbed CH_4, facilitating its release into the free phase and thereby markedly enhancing the overall gas recovery efficiency.

3.1.2. CH_4 dynamic desorption process

Once the shale sample is saturated with CH_4, a desorption experiment is initiated through the outlet end, with real-time monitoring of the shale core using NMR. Additionally, the volume of gas produced over time is measured as it exits the outlet. Traditional methods for evaluating shale production typically focus on the cumulative gas volume produced, but these methods cannot differentiate between or quantify gas volumes originating from adsorbed gas versus free gas reservoirs within the shale. In contrast, NMR technology provides a significant advantage by allowing for the quantitative assessment of CH_4 in both adsorbed and free phases within the shale. This capability effectively addresses the limitations of conventional gas measurement techniques, offering more precise insights into gas distribution and recovery dynamics.

In this experiment, the T_2 spectra of methane desorption under different pressures were monitored by NMR, as shown in Fig. 8. Measurements were conducted twice at 7 and 0.1 MPa, respectively. When the pressure decreased to 7 MPa, three distinct peaks appeared in the spectrum. The long T_2 peak (corresponding to free gas) exhibited a relatively high amplitude, indicating that a large amount of free methane in shale began to desorb and release at this pressure. Meanwhile, the short T_2 and intermediate T_2 peaks were also evident, reflecting the presence of methane in adsorbed or bound states. After a period of time, a second measurement revealed a slight decrease in the long T_2 peak, suggesting that part of the free methane had been released. In contrast, the short and intermediate T_2 peaks showed relatively small changes, implying that adsorbed/bound methane was more difficult to desorb rapidly within this pressure range, and that free methane dominated the release process with a relatively fast desorption rate (Guo et al., 2007).

When the pressure further decreased to 0.1 MPa, compared with the second test at 7 MPa, the amplitude of the long T_2 peak (free gas) was markedly reduced, indicating that more free methane was released at lower pressure. At the same time, the intermediate and short T_2 peaks remained visible, suggesting that during the 0.1 MPa stage, the desorption of adsorbed and bound methane gradually became dominant. This was manifested by a progressive reduction in the short T_2 peaks (0.1–10 ms), accompanied by a slower release rate. Ultimately, as the pressure stabilized at 0.1 MPa, the intensity of all peaks further decreased, and methane in different states was nearly completely desorbed, reaching equilibrium. In summary, when the pressure was reduced to 7 MPa, free methane was first released in large quantities, as evidenced by the rapid decline in the long T_2 peak over time. As the pressure dropped further to 0.1 MPa, methane associated with the intermediate and short T_2 peaks was also significantly desorbed, approaching complete release. Throughout the pressure-depletion desorption process, pore structure and adsorption strength were the key factors determining the desorption rate: free gas in large pores and fractures was released first (with a rapid drop in peak amplitude), whereas bound and adsorbed gas in nanopores required lower pressure and longer time to be fully desorbed.

Fig. 9 presents a schematic plot showing the recovery factors for both adsorbed and free gas as a function of production time during the methane desorption process. The recovery factors for both gas types steadily increase as the desorption time progresses. In the early stage (approximately 0–200 h), both adsorbed and free gas recovery factors rise rapidly. However, the rate of increase slows significantly over time, and the recovery approaches a stable equilibrium. At equilibrium, the recovery factor for free gas is slightly higher (approximately 85%) than that for adsorbed gas (approximately 75%). During the shale gas desorption process, the reservoir pressure continuously declines as gas is produced. In the initial phase, when the reservoir pressure is relatively high, the driving pressure differential is large, leading to high initial production rates. Both adsorbed and free gas contribute to production through desorption and diffusion, but the production rate of free gas is generally higher, particularly at the start. This is because free

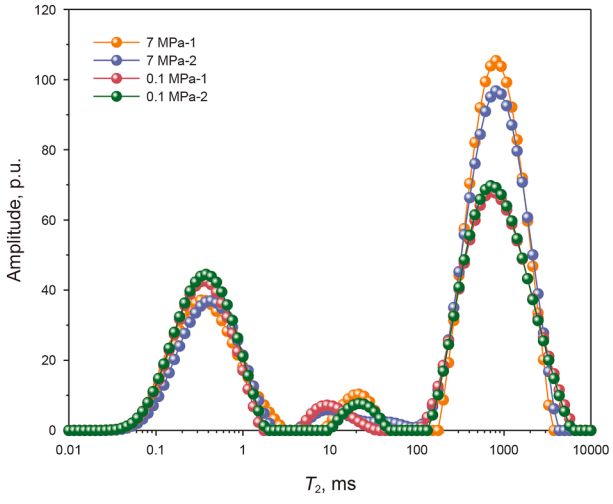

Fig. 8. T_2 spectra at different pressures during the CH_4 desorption process. 7 MPa-1: first at 7 MPa; 7 MPa-2: post-equilibration repeat at 7 MPa; 0.1 MPa-1: first at 0.1 MPa; 0.1 MPa-2: post-equilibration repeat at 0.1 MPa.

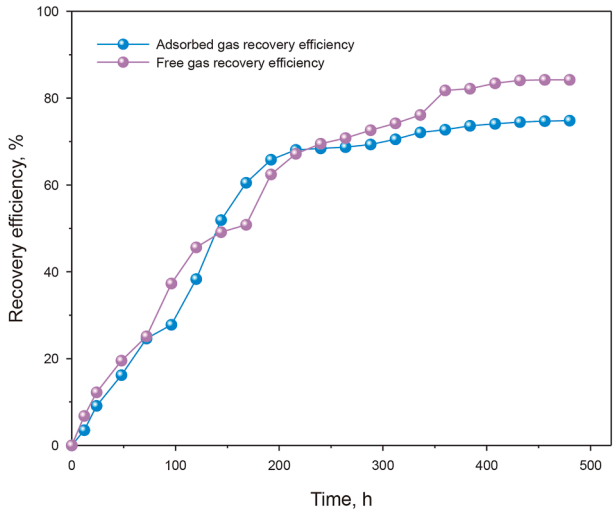

Fig. 9. Recovery rate of adsorbed gas and free gas over time.

gas, residing primarily in the pore and fracture network, has higher mobility and is more easily expelled under the pressure gradient. The slightly lower final recovery factor for adsorbed gas is attributed to the stronger surface interactions (such as van der Waals forces) that bind it to the shale matrix. These interactions make desorption slower and more kinetically limited, resulting in a lower recovery of adsorbed gas compared to the more mobile free gas.

3.2. Transformation characteristics of adsorbed-phase and free-phase methane before and after CO_2 injection

3.2.1. CH_4 secondary adsorption process

Following the completion of methane desorption, methane was re-injected into the shale sample at various pressures in preparation for the subsequent CO_2–CH_4 competitive adsorption experiment. Fig. 10 illustrates the T_2 spectra during CH_4 adsorption in shale, which typically show two main peak regions: a short T_2 peak and a long T_2 peak. The short T_2 peak is generally associated with methane that is strongly adsorbed onto surfaces or confined within nanopores, while the long T_2 peak is linked to relatively 'free' methane in larger pores, natural fractures, or loosely connected pore spaces.

As the injection pressure increases, both peak amplitudes rise, indicating a higher total methane content within the shale sample. This signifies an increase in both adsorbed and free-phase methane volumes, progressively filling pore spaces at various scales. At the maximum pressure (10 MPa, represented by the green curve), both peaks reach their maximum amplitudes, indicating the shale has reached its maximum methane saturation under these conditions. The short T_2 peak becomes progressively higher and sharper as the pressure increases, reflecting a significant rise in methane adsorbed on the surfaces of the shale matrix and within nanopores. This methane fraction interacts most strongly with the pore surfaces, resulting in a marked increase in adsorption capacity as the pressure rises. Similarly, the long T_2 peak amplitude grows with increasing pressure, representing an increase in the free-phase methane within larger pores or microfractures. This peak also exhibits some positional shifts with varying pressure, likely reflecting changes in the density and fluid properties of methane within these larger pore spaces.

Fig. 11 shows the change in the total NMR peak area over time (represented by sampling number) during this secondary CH_4 adsorption process. The peak area shows an overall increasing trend as the experiment progresses, initially fluctuating, followed by a steady rise, and then leveling off towards stability. This suggests a progressive increase in methane content as the shale adsorbs methane from the surrounding gas environment, gradually reaching higher saturation over time. The observed local decreases or fluctuations in the peak area curve may be attributed to several factors, including minor pressure adjustments, temperature variations, the timing of sampling intervals, inherent measurement repeatability errors, and the heterogeneity of the shale sample. Some pores may fill more quickly than others, particularly micropores or those within complex pore networks, which may explain the variations in peak area between consecutive sampling intervals.

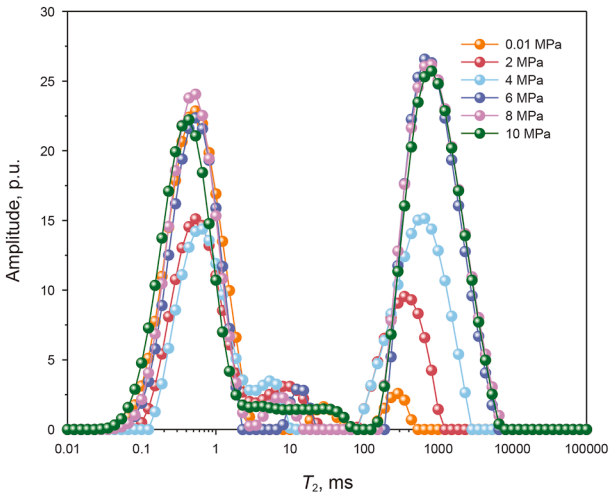

Fig. 10. T_2 spectra during the CH_4 secondary adsorption process.

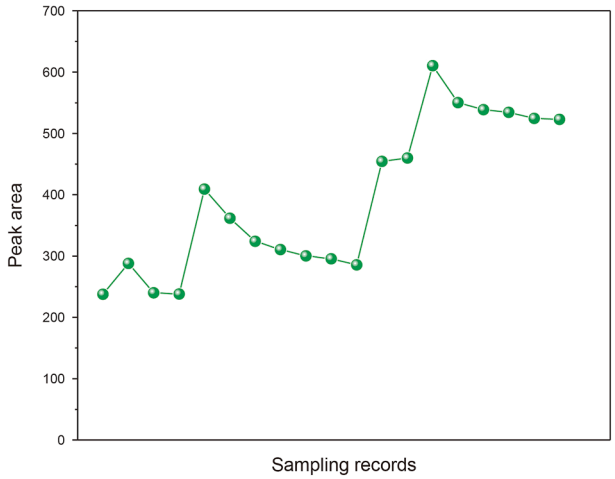

Fig. 11. Peak areas of the CH_4 secondary adsorption process at different sampling intervals.

3.2.2. CO_2–CH_4 competitive adsorption effect and mechanism

According to Gibbs adsorption theory (Donohue and Aranovich, 1998), shale pore surfaces, particularly those enriched in organic matter, typically exhibit a strong adsorption capacity for gases. Upon CO_2 injection, the molecular properties of CO_2—such as its polarity, molecular size, and intermolecular forces—give it a stronger affinity for shale surfaces compared to CH_4. As a result, CO_2 molecules can more easily displace CH_4 molecules that were previously adsorbed, leading to competitive adsorption. In addition, the injection of CO_2 significantly alters the composition of the free gas phase within the pores, leading to a sharp decline in the mole fraction of CH_4. According to Dalton's law of partial pressures (Hilgeman et al., 2007), this reduction lowers the partial pressure of CH_4, thereby disrupting the original gas–solid equilibrium and providing additional driving force for the further desorption of adsorbed CH_4. This process is referred to as the component-stripping effect. This reduction in CH_4 partial pressure increases the concentration of desorbed methane within the pores and fractures. The liberated methane then undergoes flow, diffusion, and migration towards production wells or other lower-pressure regions (Cao et al., 2025), as illustrated in Fig. 12. Thus, injecting high-pressure CO_2 into shale not only enhances shale gas production by promoting the desorption of CH_4, but also improves the overall recovery factor. Simultaneously, this process contributes to the geological sequestration of CO_2, serving a dual purpose in both gas recovery and CO_2 storage.

NMR technology allows for the detection of hydrogen atoms in methane within shale, while CO_2, which lacks hydrogen atoms,

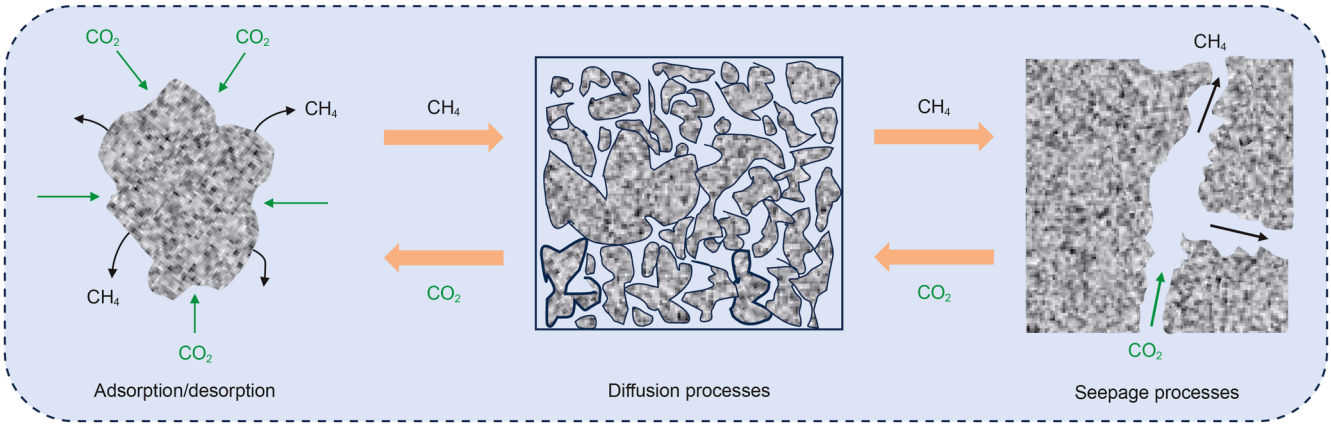

Fig. 12. Schematic of CO_2–CH_4 competitive adsorption/desorption–diffusion–seepage in shale.

does not generate an NMR signal. This makes NMR an effective tool for studying the competitive adsorption dynamics between CO_2 and CH_4, as changes in the T_2 spectral signal intensity reflect variations in methane content. In the experiment, the shale sample was first saturated with CH_4 at 10 MPa to achieve dynamic adsorption equilibrium. Then, CO_2 at 15 MPa was injected into the CH_4-saturated sample, initiating competitive adsorption between the two gases, particularly on pore surfaces, including organic matter pores. NMR T_2 spectra were acquired at various time points during the CO_2 injection to monitor the changes in methane content and phase distribution within the shale pores. The evolution of the methane signal was tracked by analyzing the T_2 peak areas, with results shown in Figs. 13 and 14.

Fig. 13 illustrates the changes in the T_2 spectra. The short T_2 peak, associated with adsorbed methane in micro-/nanopores or on organic matter surfaces, shows a decrease in amplitude and a possible shift after CO_2 injection. This indicates that methane originally adsorbed in these tightly bound locations has been displaced or "squeezed" out by CO_2, which has a higher adsorption affinity. The long T_2 peak, representing free-phase methane in larger pores or fractures, exhibits a slight increase in amplitude and a rightward shift during CO_2 injection. This suggests that displaced methane migrates into larger pores or fractures, which may enhance its recovery. These spectral changes reflect a

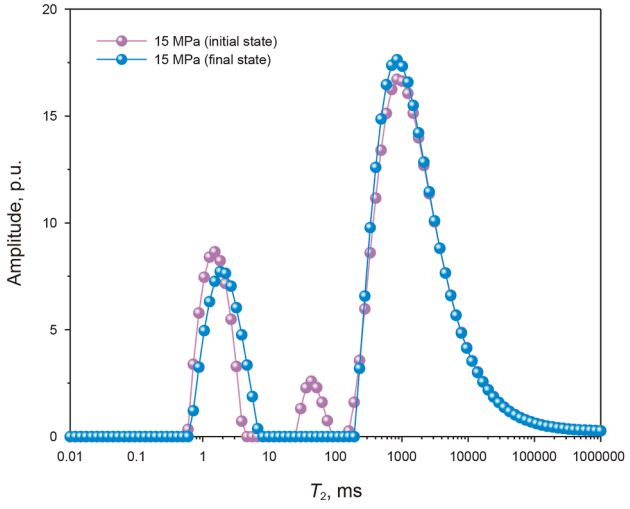

Fig. 13. T_2 spectra of methane during the CO_2 injection process.

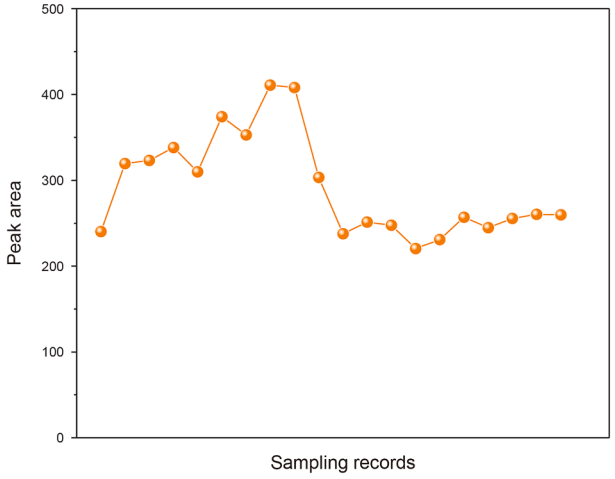

Fig. 14. Peak areas during the CO_2 injection process at different sampling intervals.

transition in methane's occurrence state, with CO_2 preferentially adsorbing onto nanopore surfaces and displacing methane to larger, more recoverable pore spaces (Wang et al., 2023). Fig. 14 shows the evolution of the total peak area over time during CO_2 injection. The peak area initially rises, then decreases, and fluctuates before stabilizing at a lower level. This trend reflects the displacement of methane during the competitive adsorption process. The initial rise could be due to pressure disturbances or pore fluid redistribution, temporarily making fluid signals from previously inaccessible pores more visible. As the competitive adsorption effect becomes dominant, methane is displaced and migrates to spaces where it may be lost or redistributed, causing the total methane signal to decrease. The stabilization of the peak area at later times indicates that the CO_2–CH_4 competitive adsorption process is approaching equilibrium, with CO_2 occupying more adsorption sites and methane remaining in larger pores. Collectively, the CO_2 injection process enhances methane desorption and recovery while simultaneously sequestering CO_2 within the shale, creating a "win-win" scenario that improves gas recovery and contributes to CO_2 storage.

Based on a comprehensive analysis, this dynamic trend in total methane signal, as quantified in Fig. 14, reflects the underlying microscopic phase transitions that occur throughout the competitive adsorption process. The initial fluctuations and subsequent steady decline in the total peak area correspond directly to the

progressive displacement of CH_4 from adsorption sites. To visualize the net effect of this entire process on methane's phase distribution, Fig. 13 provides a direct comparison of the T_2 spectra before and after CO_2 injection reached equilibrium. The transformation from the initial state (15 MPa (initial state)) to the final state (15 MPa (final state)) in Fig. 13 is, in essence, the cumulative result of the continuous signal evolution shown in Fig. 14. Specifically, the steady decrease in the total signal observed in Fig. 14 is primarily driven by the reduction of the short-T_2 peak, confirming that the displacement of adsorbed CH_4 is the dominant mechanism. In addition, our NMR results confirm competitive adsorption at the pore scale, but the molecular-level mechanisms remain unresolved by this technique. We propose that future work should integrate these experiments with molecular simulations (MD/MC) to quantify fundamental parameters like adsorption selectivity and nanopore diffusion. This combined "experiment-simulation" approach is essential for providing a deeper, atomistic interpretation of our T_2 spectral data and for building more accurate predictive reservoir models.

3.3. Effect of CO_2 injection on enhancing CH_4 desorption

After the completion of CO_2 competitive adsorption in the CH_4-saturated shale sample, the outlet valve was opened to initiate depressurization and gas desorption. Due to the prior CO_2 injection, the desorption kinetics and phase distribution of methane during pressure reduction were expected to differ from the scenario without CO_2 injection. Fig. 15 shows that, compared to the desorption scenario without prior CO_2 injection, the height and area of the short T_2 peak are noticeably reduced. This suggests that the CO_2 injection has displaced or expelled some of the methane originally adsorbed strongly in micropores or on organic matter surfaces. As a result, this methane has migrated to more accessible locations, making it easier to desorb or mobilize. At a pressure of 7 MPa, T_2 spectra were recorded at different time points (labeled 7 MPa-1 to 7 MPa-5). While the position of the short T_2 peak remains largely unchanged, its height and shape evolve over time. After the initial pressure reduction, CO_2's occupation of strong adsorption sites means that less strongly bound CH_4 remains, and the redistribution of CO_2 and CH_4 continues towards equilibrium under the new pressure conditions. This leads to a gradual stabilization of the short T_2 peak after some initial changes. Additionally, smaller peaks or shoulders are observed in the medium/long T_2 regions (around 10, 100, and 1000 ms). These peaks appear relatively stronger after the CO_2 injection and subsequent pressure reduction to 7 MPa compared to the initial CH_4-saturated state. This indicates that methane displaced from micropores by CO_2 has accumulated in larger pores or fractures. However, at 7 MPa, the pressure is not low enough to release all of the free-phase gas in these larger pores. Instead, it primarily leads to redistribution of methane across different pore sizes.

Fig. 16 illustrates the T_2 spectra during the final desorption phase down to 0.1 MPa, following CO_2 injection. By comparing the measurements taken after stabilizing at 0.1 MPa for 20 min (0.1 MPa, orange curve) and 30 min (0.1 MPa, green curve), it is evident that the amplitude of the short T_2 peak remains relatively prominent in both cases, although there are slight differences between the two time points. A lower peak amplitude in the later measurement (0.1 MPa, green curve) indicates continued desorption of adsorbed CH_4 over the extended stabilization time. Conversely, a slightly higher peak might suggest that during pore fluid redistribution, some locally trapped methane becomes more detectable in the short T_2 range. Regardless of these minor temporal variations, the overall amplitude of the entire spectrum at 0.1 MPa is significantly lower than in the initial saturated state, confirming substantial desorption. Focusing on the medium/long T_2 peaks and the spectral tail, methane in larger pores or the free phase is expected to be readily released at this low pressure (0.1 MPa). Consequently, these peaks are typically very small or nearly absent. Any residual peaks in these regions suggest that some methane has not been completely expelled, potentially due to trapping within dead-end pores or fractures (Klewiah et al., 2020; Zhou et al., 2019). Crucially, when compared to the direct depressurization process conducted without prior CO_2 injection, the extent of desorption is significantly higher after the CO_2 treatment, as evidenced by the lower overall intensity of the T_2 spectrum. By the time the pressure reaches 0.1 MPa, methane desorption is nearly complete, leaving only a small residual amount in the shale. This indicates that CO_2 injection facilitates the displacement and subsequent release of methane that was originally strongly adsorbed. Under the combined effects of CO_2 competitive adsorption and the low-pressure environment, most of the methane displaced by CO_2 is produced over time, enhancing overall CH_4 recovery efficiency. This contrasts with the desorption

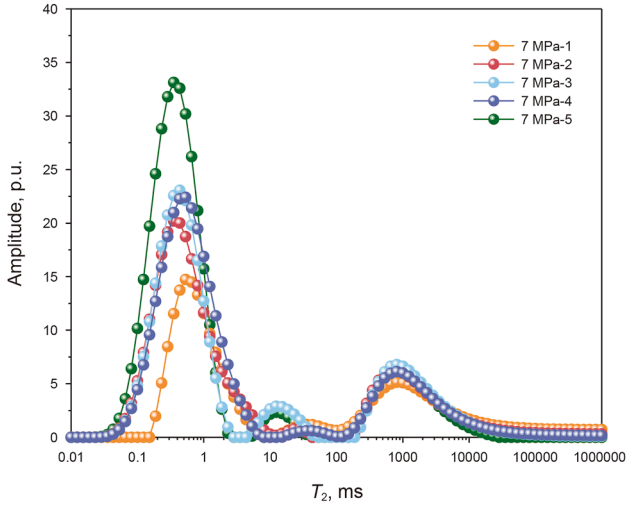

Fig. 15. T_2 spectra during CH_4 desorption after CO_2 injection at 7 MPa. 7 MPa-1: free-gas rapid release; 7 MPa-2: early desorption, adsorbed gas responding; 7 MPa-3 and 7 MPa-4: active desorption, major supplement; 7 MPa-5: peak stage, dominant mechanism.

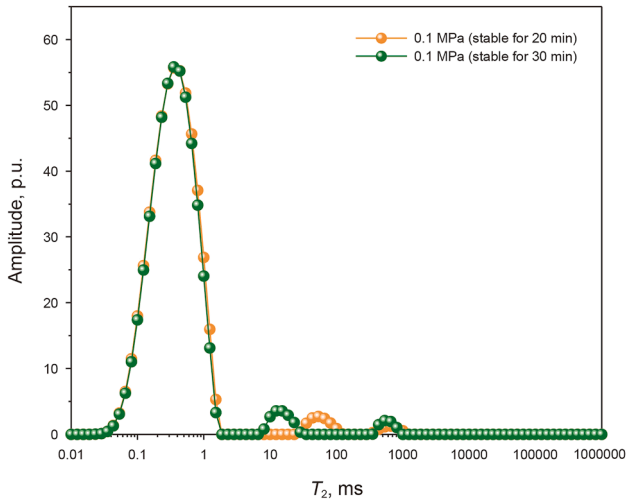

Fig. 16. T_2 spectra during CH_4 re-desorption after CO_2 injection at 0.1 MPa.

behavior during direct methane depressurization, where the reduction in the large-pore signal may be less complete due to residual trapping. The CO_2-enhanced process not only significantly reduces the amount of adsorbed methane but also facilitates more thorough desorption from the larger pore spaces, leading to near-complete methane removal.

In the CO_2-CH_4 depressurization desorption experiment, gas chromatography (GC) was used to measure the concentrations of CH_4 and CO_2 in the produced gas at various equilibrium pressures. Fig. 17 shows the characteristic changes in gas content during the desorption process as the pressure decreases: Initial phase (0–200 h): CO_2 primarily drives CH_4 desorption. CO_2 occupies pore spaces, and CH_4 is displaced and released, with minimal CO_2 production. Intermediate phase (200–400 h): The rate of CH_4 release slows as the readily desorbable methane depletes. CO_2 continues to displace CH_4, and CO_2 production increases. Later phase (beyond 400 h): CO_2 release sharply increases, demonstrating the efficiency of CO_2 in displacing CH_4 and its sequestration within the reservoir. These results highlight the effectiveness of CO_2–CH_4 displacement in improving shale gas recovery and emphasize the potential of shale reservoirs for CO_2 sequestration and carbon emission reduction (Rani et al., 2019).

To quantitatively assess the enhancement of CH_4 desorption efficiency by CO_2 injection, the desorption efficiency was calculated using NMR peak areas measured during the desorption process following CO_2 injection. Fig. 18 compares the desorption efficiency achieved with CO_2 injection to that under simple pressure depletion (without prior CO_2 injection) at pressures of 7 and 0.1 MPa. Without CO_2 injection (natural depressurization), the CH_4 desorption efficiencies were 62.9% at 7 MPa and 67.2% at 0.1 MPa, indicating that over 30% of methane remained in the shale; with CO_2 injection, desorption efficiencies increased to 73.1% at 7 MPa and 77.9% at 0.1 MPa. This represents an overall increase of about 10%. The enhanced desorption efficiency following CO_2 injection is attributed to the competitive adsorption effect between CO_2 and CH_4. This is consistent with previous research trends (Ding et al., 2022; Tang et al., 2023). CO_2, with a higher adsorption affinity for organic matter surfaces, displaces methane, which then migrates to larger pores or fractures where it can be more easily released during subsequent pressure reduction. These results demonstrate that CO_2 injection significantly improves methane desorption efficiency, confirming the potential of CO_2–CH_4 competitive adsorption to enhance shale gas recovery.

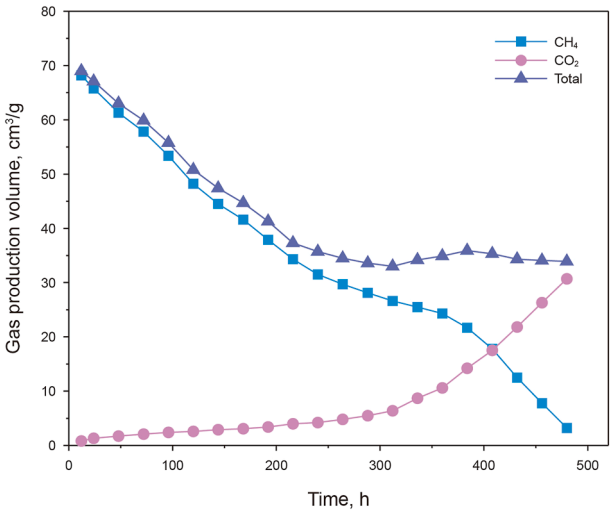

Fig. 17. CH_4 and CO_2 content versus time during desorption.

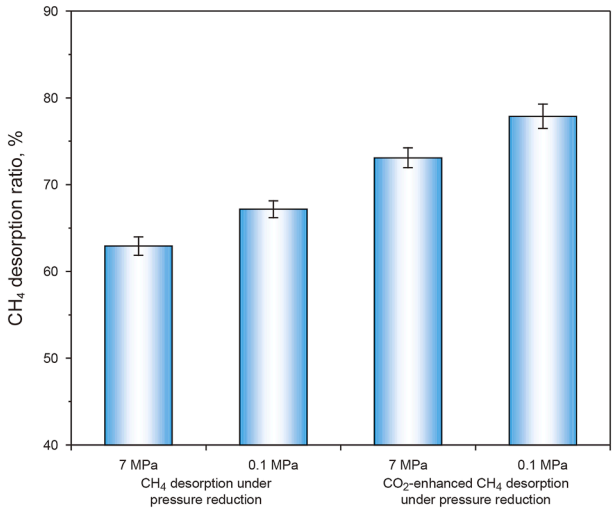

Fig. 18. Comparison of CH_4 desorption under pressure reduction with and without CO_2 injection.

3.4. Significance of CO_2-ESGR and carbon sequestration

The combined application of CO_2-ESGR and carbon sequestration (CS) offers significant potential for both energy development and environmental protection (Joeng et al., 2023; Liu et al., 2025; Wang et al., 2025). This study utilized low-field NMR to dynamically monitor methane adsorption and desorption behavior in shale, providing insights into the changes in methane's occurrence state (phase distribution) before and after CO_2 injection. NMR analysis revealed a notable decrease in signal intensity in the short T_2 region, corresponding to adsorbed CH_4, and an increase in the long T_2 region, representing free-phase CH_4, after CO_2 injection. This confirms that CO_2 effectively displaces adsorbed methane through competitive adsorption, promoting its transition to the free phase and increasing shale gas recovery potential.

Quantitative recovery factor calculations showed a significant boost in production efficiency for both adsorbed and free gas, with the greatest improvement observed in adsorbed methane recovery. These findings validate that the CO_2 competitive adsorption mechanism not only enhances methane recovery but also improves the economic viability of shale gas development, highlighting the practical significance of CO_2-ESGR technology. Furthermore, NMR was used to monitor changes in gas composition following CO_2 injection. Experimental data demonstrated that as methane was released, CO_2 progressively increased in proportion and stabilized, occupying a substantial fraction of the shale's adsorption sites. This shows the preferential adsorption of CO_2 and its favorable storage capacity, providing evidence for effective CO_2 sequestration within the shale matrix. The observation that CO_2 release eventually surpasses methane release further supports the long-term effectiveness and stability of shale formations as CO_2 repositories, reinforcing the role of this technology in carbon emission reduction. The NMR experimental results underscore the dual benefits of CO_2-ESGR technology: enhanced methane recovery and effective CO_2 sequestration (Chang et al., 2024; Xu C. et al., 2024). On one hand, the improved methane recovery rate enhances the economic viability of shale gas fields and extends their production lifespan. On the other hand, the effective geological sequestration of CO_2 contributes significantly to reducing greenhouse gas emissions, supporting global carbon emission reduction targets. Although challenges such as high costs and monitoring difficulties may arise during field-scale implementation, this study

provides solid experimental evidence demonstrating the technology's economic and environmental value, offering a strong foundation for future large-scale applications.

In summary, this research demonstrates the practical value of using NMR technology to characterize the CO_2-ESGR and carbon sequestration process, elucidating the microscopic mechanisms of CO_2 competitive adsorption and confirming CO_2 sequestration effectiveness. With further technological optimization and field demonstrations, CO_2-ESGR technology is poised to play a key role in both efficient shale gas production and global carbon emission reduction efforts.

4. Conclusions

This study utilized low-field NMR technology to dynamically monitor the adsorption and desorption processes of methane in shale in real-time, demonstrating the method's effectiveness in distinguishing between adsorbed and free-phase methane. The analysis of T_2 spectra and peak areas under varying pressures provided a robust foundation for quantitatively assessing shale gas recovery efficiency. Results indicated that while the volume of adsorbed methane remained relatively stable, the volume of free-phase methane within fractures and larger pores increased significantly as the injection pressure rose, highlighting distinct pressure-dependent changes in methane's occurrence state within the shale.

Competitive adsorption experiments involving CO_2 injection confirmed that CO_2, with its higher adsorption affinity, effectively displaces adsorbed methane, promoting the transition of methane to the free phase and enhancing desorption efficiency. Comparative analysis of depressurization desorption experiments revealed a marked increase in methane desorption efficiency following CO_2 injection under identical conditions. Additionally, NMR data confirmed the long-term stable presence of the injected CO_2 within the shale, indicating its strong geological sequestration capacity. These findings demonstrate the technical feasibility of CO_2-ESGR and provide experimental evidence supporting carbon capture and sequestration. This method not only improves methane recovery efficiency but also has significant carbon dioxide storage potential, fully demonstrating the dual advantages of this technology and providing valuable guidance for practical engineering applications and the optimization of carbon emission reduction strategies.

Although this study successfully elucidates the fundamental mechanisms of CO_2–CH_4 competitive adsorption at the microscale, we acknowledge a critical limitation regarding the experimental conditions. All measurements were conducted at room temperature, which does not fully replicate the elevated temperatures (e.g., ~100 °C) characteristic of deep shale reservoirs. A key implication is that injected CO_2 would exist in a supercritical state under in situ conditions, whose unique transport properties may enhance its ability to penetrate the intricate nanopore network of shale and more effectively displace adsorbed methane. Looking ahead, a critical next step is to conduct comparable nuclear magnetic resonance (NMR) monitoring experiments on shale samples of different maturity levels under simulated high-temperature and high-pressure reservoir conditions. Such investigations will enable dynamic tracking of the competitive displacement process involving supercritical carbon dioxide, thereby bridging the gap between laboratory-scale understanding and field-scale engineering applications. Ultimately, this will provide more reliable and optimized strategies for achieving the dual objectives of enhancing natural gas recovery and ensuring efficient carbon sequestration.

CRediT authorship contribution statement

Sheng-Ming Huang: Writing – original draft, Methodology, Investigation, Data curation. **Guan-Cheng Jiang:** Supervision, Resources, Project administration, Funding acquisition. **Jun Yang:** Methodology, Investigation. **Chun-Ping Guo:** Methodology, Investigation. **Quan-De Wang:** Writing – review & editing, Investigation. **Teng-Fei Dong:** Writing – review & editing. **Yin-Bo He:** Writing – review & editing, Investigation. **Li-Li Yang:** Writing – review & editing, Methodology. **Qing-Gong Liu:** Investigation. **Zhe-Hui Jin:** Supervision, Project administration, Funding acquisition.

Data availability

Data will be made available on request.

Declaration of interests

The authors declare that they have no known competing financial interests or personal relationships that could have appeared to influence the work reported in this paper.

Acknowledgment

This work was financially supported by the National Natural Science Foundation of China (Major Support Program, No. U23B2082). The authors also gratefully acknowledge a Discovery Grant from the Natural Sciences and Engineering Research Council of Canada (NSERC RGPIN-2023-03587). Additionally, the authors gratefully acknowledge financial support from the China Scholarship Council (No. 202406440019).

References

Ahn, Y., Kim, J., Kwon, J., 2020. Optimal design of supply chain network with carbon dioxide injection for enhanced shale gas recovery. Appl. Energy 274, 115334. https://doi.org/10.1016/j.apenergy.2020.115334.

Bai, Y., Lin, H., Li, S., et al., 2021. Molecular simulation of N_2 and CO_2 injection into a coal model containing adsorbed methane at different temperatures. Energy 219, 119686. https://doi.org/10.1016/j.energy.2020.119686.

Brochard, L., Vandamme, M., Pellenq, R., et al., 2012. Adsorption-induced deformation of microporous materials: Coal swelling induced by CO_2–CH_4 competitive adsorption. Langmuir 28 (5), 2659–2670. https://doi.org/10.1021/la204072d.

Cao, M., Qin, C., Jiang, Y., et al., 2025. Review of competitive adsorption of CO_2/CH_4 in shale: Implications for CO_2 sequestration and enhancing shale gas recovery. ACS Omega 10 (13), 12756–12771. https://doi.org/10.1021/acsomega.4c08678.

Chang, X., Lin, S., Yang, C., et al., 2024. A critical review of $ScCO_2$-enhanced gas recovery and geologic storage in shale reservoirs. Gas Sci. Eng. 125, 205317. https://doi.org/10.1016/j.jgsce.2024.205317.

Chen, L., Zuo, L., Jiang, Z., et al., 2019. Mechanisms of shale gas adsorption: Evidence from thermodynamics and kinetics study of methane adsorption on shale. Chem. Eng. J. 361, 559–570. https://doi.org/10.1016/j.cej.2018.11.185.

Cooper, J., Stamford, L., Azapagic, A., 2018. Economic viability of UK shale gas and potential impacts on the energy market up to 2030. Appl. Energy 215, 577–590. https://doi.org/10.1016/j.apenergy.2018.02.051.

Ding, J., Yan, C., Wang, G., et al., 2022. Competitive adsorption between CO_2 and CH_4 in tight sandstone and its influence on CO_2-injection enhanced gas recovery (EGR). Int. J. Greenh. Gas Control 113, 103530. https://doi.org/10.1016/j.ijggc.2021.103530.

Donohue, M., Aranovich, G., 1998. Classification of Gibbs adsorption isotherms. Adv. Colloid Interface Sci. 76–77, 137–152. https://doi.org/10.1016/S0001-8686(98)00044-X.

Feng, D., Chen, Z., Wu, K., et al., 2022. A comprehensive review on the flow behaviour in shale gas reservoirs: Multi-scale, multi-phase, and multi-physics. Can. J. Chem. Eng. 100, 3084–3122. https://doi.org/10.1002/cjce.24439.

Feng, Q., Xu, S., Xing, X., et al., 2020. Advances and challenges in shale oil development: A critical review. Adv. Geo-Energy Res. 4 (4), 406–418. https://doi.org/10.46690/ager.2020.04.06.

Feng, Z., Hao, F., Tian, J., et al., 2022. Shale gas geochemistry in the Sichuan Basin, China. Earth Sci. Rev. 232, 104141. https://doi.org/10.1016/j.earscirev.2022.104141.

Guo, R., Mannhardt, K., Kantzas, A., 2007. Characterizing moisture and gas content of coal by low-field NMR. J. Can. Pet. Technol. 46 (10). https://doi.org/10.2118/07-10-05.
Guo, S., 2013. Experimental study on isothermal adsorption of methane gas on three shale samples from upper Paleozoic strata of the ordos basin. J. Petrol. Sci. Eng. 110, 132–138. https://doi.org/10.1016/j.petrol.2013.08.048.
Hilgeman, F.R., Wilson, B., Bertrand, G., 2007. Using Dalton's law of partial pressures to determine the vapor pressure of a volatile liquid. J. Chem. Educ. 84 (3), 469. https://doi.org/10.1021/ed084p469.
Hu, K., Zhang, Q., Liu, Y., et al., 2023. A developed dual-site langmuir model to represent the high-pressure methane adsorption and thermodynamic parameters in shale. Int. J. Coal Sci. Technol 10, 59. https://doi.org/10.1007/s40789-023-00629-x.
Huang, L., Ning, Z., Wang, Q., et al., 2018. Effect of organic type and moisture on CO_2/CH_4 competitive adsorption in kerogen with implications for CO_2 sequestration and enhanced CH_4 recovery. Appl. Energy 210, 28–43. https://doi.org/10.1016/j.apenergy.2017.10.122.
Huang, S., Jiang, G., Guo, C., et al., 2024. Experimental study of adsorption/desorption and enhanced recovery of shale oil and gas by zwitterionic surfactants. Chem. Eng. J. 487, 150628. https://doi.org/10.1016/j.cej.2024.150628.
Huang, S., Jiang, G., Chang, Z., et al., 2025. The effect of viscoelastic surfactant fracturing fluid on methane adsorption/desorption characteristics in shale: Experimental and mechanistic study. Chem. Eng. J. 510, 161901. https://doi.org/10.1016/j.cej.2025.161901.
Huang, X., Zhao, Y., 2017. Characterization of pore structure, gas adsorption, and spontaneous imbibition in shale gas reservoirs. J. Petrol. Sci. Eng. 159, 197–204. https://doi.org/10.1016/j.petrol.2017.09.010.
Jiang, G., Sun, J., He, Y., et al., 2022. Novel water-based drilling and completion fluid technology to improve wellbore quality during drilling and protect unconventional reservoirs. Engineering 18, 129–142. https://doi.org/10.1016/j.eng.2021.11.014.
Joeng, S., Park, J., Lee, J., et al., 2023. Review of the adsorption equilibria of CO_2, CH_4, and their mixture on coals and shales at high pressures for enhanced CH_4 recovery and CO_2 sequestration. Fluid Phase Equilib. 564, 113591. https://doi.org/10.1016/j.fluid.2022.113591.
Kausik, R., Fellah, K., Rylander, E., et al., 2016. NMR relaxometry in shale and implications for logging. Petrophysics 57 (4), 339–350. SPWLA-2016-v57n4a1.
Kerr, R., 2010. Natural gas from shale bursts onto the scene. Science 328 (5986), 1624–1626. https://doi.org/10.1126/science.328.5986.1624.
Kleinberg, R., Vinegar, H., 1996. NMR properties of reservoir fluids. Log. Anal. 37 (6), 20–32.
Kleinberg, R., Farooqui, S., Horsfield, M., 1993. T_1/T_2 ratio and frequency dependence of NMR relaxation in porous sedimentary rocks. J. Colloid Interface Sci. 158, 195–198. https://doi.org/10.1006/jcis.1993.1247.
Klewiah, I., Berawala, D., Walker, H., et al., 2020. Review of experimental sorption studies of CO_2 and CH_4 in shales. J. Nat. Gas Sci. Eng. 73, 103045. https://doi.org/10.1016/j.jngse.2019.103045.
Li, X., Huang, W., Sun, J., et al., 2024. NMR investigation of methane hydrate formation and dissociation behavior induced by heat flow in sandy porous media. Energy & Fuels 38, 5834–5846. https://doi.org/10.1021/acs.energyfuels.3c04825.
Li, Y., Li, Y., Wang, B., et al., 2016. The status quo review and suggested policies for shale gas development in China. Renew. Sustain. Energy Rev. 59, 420–428. https://doi.org/10.1016/j.rser.2015.12.351.
Liao, Q., Zhou, J., Xian, X., et al., 2023. Competition adsorption of CO_2/CH_4 in shale: Implications for CO_2 sequestration with enhanced gas recovery. Fuel 339, 127400. https://doi.org/10.1016/j.fuel.2023.127400.
Liu, A., Liu, S., Zhang, K., et al., 2025. Competitive sorption of CH_4 and CO_2 on coals: Implications for carbon geo-storage. Sep. Purif. Technol. 354, 129399. https://doi.org/10.1016/j.seppur.2024.129399.
Liu, D., Agarwal, R., Li, Y., 2017. Numerical simulation and optimization of CO_2 enhanced shale gas recovery using a genetic algorithm. J. Clean. Prod. 164, 1093–1104. https://doi.org/10.1016/j.jclepro.2017.07.040.
Liu, J., Xie, L., Elsworth, D., et al., 2019. CO_2/CH_4 competitive adsorption in shale: Implications for enhancement in gas production and reduction in carbon emissions. Environ. Sci. Technol. 53 (15), 9328–9336. https://doi.org/10.1021/acs.est.9b02432.
Liu, L., Nicholson, D., Bhatia, S., 2015. Adsorption of CH_4 and CH_4/CO_2 mixtures in carbon nanotubes and disordered carbons: A molecular simulation study. Chem. Eng. Sci. 121, 268–278. https://doi.org/10.1016/j.ces.2014.07.041.
Liu, S., Zhang, Y., Xing, W., et al., 2015. Laboratory experiment of CO_2–CH_4 displacement and dispersion in sandpacks in enhanced gas recovery. J. Nat. Gas Sci. Eng. 26, 1585–1594. https://doi.org/10.1016/j.jngse.2015.04.021.
Lu, T., Zeng, K., Jiang, P., et al., 2022. Competitive adsorption in CO_2 enhancing shale gas: Low-field NMR measurement combined with molecular simulation for selectivity and displacement efficiency model. Chem. Eng. J. 440, 135865. https://doi.org/10.1016/j.cej.2022.135865.
Lu, Z., Li, K., Liu, X., et al., 2023. Low-field NMR application in the characterization of CO_2 geological storage and utilization related to shale gas reservoirs: A brief review. Front. Earth Sci. 17 (3), 739–751. https://doi.org/10.1007/s11707-022-1007-0.
Lutz, B., Lewis, A., Doyle, M., 2013. Generation, transport, and disposal of wastewater associated with Marcellus Shale gas development. Water Resour. Res. 49, 647–656. https://doi.org/10.1002/wrcr.20096.
Ma, H., Yang, Y., Zhang, Y., et al., 2022. Optimized schemes of enhanced shale gas recovery by CO_2-N_2 mixtures associated with CO_2 sequestration. Energy Convers. Manag. 268, 116062. https://doi.org/10.1016/j.enconman.2022.116062.
Ma, Y., Cai, X., Zhao, P., 2018. China's shale gas exploration and development: Understanding and practice. Petrol. Explor. Dev. 45 (4), 589–603. https://doi.org/10.1016/S1876-3804(18)30065-X.
Merey, S., 2019. Analysis of the effect of experimental adsorption uncertainty on CH_4 production and CO_2 sequestration in Dadas shale gas reservoir by numerical simulations. J. Petrol. Sci. Eng. 178, 1051–1066. https://doi.org/10.1016/j.petrol.2019.04.022.
Mohagheghian, E., Hassanzadeh, H., Chen, Z., 2019. CO_2 sequestration coupled with enhanced gas recovery in shale gas reservoirs. J. CO_2 Util. 34, 646–655. https://doi.org/10.1016/j.jcou.2019.08.016.
Omari, A., Wang, C., Li, Y., et al., 2022. The progress of enhanced gas recovery (EGR) in shale gas reservoirs: A review of theory, experiments, and simulations. J. Petrol. Sci. Eng. 213, 110461. https://doi.org/10.1016/j.petrol.2022.110461.
Qin, C., Jiang, Y., Cao, M., et al., 2023. Experimental study on the methane desorption-diffusion behavior of Longmaxi shale exposure to supercritical CO_2. Energy 262, 125456. https://doi.org/10.1016/j.energy.2022.125456.
Rani, S., Padmanabhan, E., Prusty, B., 2019. Review of gas adsorption in shales for enhanced methane recovery and CO_2 storage. J. Petrol. Sci. Eng. 175, 634–643. https://doi.org/10.1016/j.petrol.2018.12.081.
Rivard, C., Lavoie, D., Lefebvre, R., et al., 2014. An overview of Canadian shale gas production and environmental concerns. Int. J. Coal Geol. 126, 64–76. https://doi.org/10.1016/j.coal.2013.12.004.
Skytt, T., Nielsen, S., Jonsson, B., 2020. Global warming potential and absolute global temperature change potential from carbon dioxide and methane fluxes as indicators of regional sustainability–A case study of Jämtland, Sweden. Ecol. Indic. 110, 105831. https://doi.org/10.1016/j.ecolind.2019.105831.
Straley, C., Rossini, D., Vinegar, H., et al., 1997. Core analysis by low field NMR. Log. Anal. 1997 38 (2), 84–94.
Sun, C., Nie, H., Dang, W., et al., 2021. Shale gas exploration and development in China: Current status, geological challenges, and future directions. Energy & Fuels 35 (8), 6359–6379. https://doi.org/10.1021/acs.energyfuels.0c04131.
Sun, H., Yao, J., Gao, S., et al., 2013. Numerical study of CO_2 enhanced natural gas recovery and sequestration in shale gas reservoirs. Int. J. Greenh. Gas Control 19, 406–419. https://doi.org/10.1016/j.ijggc.2013.09.011.
Sun, H., Cai, X., Hu, D., et al., 2023. Theory, technology and practice of shale gas three-dimensional development: A case study of Fuling shale gas field in Sichuan Basin, SW China. Petrol. Explor. Dev. 50 (3), 651–664. https://doi.org/10.1016/S1876-3804(23)60417-3.
Sun, J., Chen, C., Zhang, Y., et al., 2022. Competitive adsorption characteristics based on partial pressure and adsorption mechanism of CO_2/CH_4 mixture in shale pores. Chem. Eng. J. 430, 133172. https://doi.org/10.1016/j.cej.2021.133172.
Sun, X., Yao, Y., Liu, D., et al., 2016. Interactions and exchange of CO_2 and H_2O in coals: An investigation by low-field NMR relaxation. Sci. Rep. 6, 19919. https://doi.org/10.1038/srep19919.
Tang, C., Zhou, W., Chen, Z., et al., 2023. Numerical simulation of CO_2 sequestration in shale gas reservoirs at reservoir scale coupled with enhanced gas recovery. Energy 277, 127657. https://doi.org/10.1016/j.energy.2023.127657.
Tang, X., Ripepi, N., Lubacher, K., et al., 2017. Adsorption models for methane in shales: Review, comparison, and application. Energy & Fuels 31 (10), 10787–10801. https://doi.org/10.1021/acs.energyfuels.7b01948.
Wang, H., Zhou, J., Xian, X., et al., 2025. Shale gas production and CO_2 storage of CO_2-ESGR based on the stress–strain–sorption behavior of shale. Energy & Fuels 39 (11), 5406–5418. https://doi.org/10.1021/acs.energyfuels.5c00489.
Wang, Q., Li, R., 2017. Research status of shale gas: A review. Renew. Sustain. Energy Rev. 74, 715–720. https://doi.org/10.1016/j.rser.2017.03.007.
Wang, Q., Chen, X., Jha, A., et al., 2014. Natural gas from shale formation–The evolution, evidences and challenges of shale gas revolution in United States. Renew. Sustain. Energy Rev. 30, 1–28. https://doi.org/10.1016/j.rser.2013.08.065.
Wang, S., Zhou, S., Pan, Z., et al., 2023. Response of pore network fractal dimensions and gas adsorption capacities of shales exposed to supercritical CO_2: Implications for CH_4 recovery and carbon sequestration. Energy Rep. 9, 6461–6485. https://doi.org/10.1016/j.egyr.2023.05.266.
Wen, H., Hao, J., Ma, L., et al., 2022. Experimental study on replacing coal seam CH_4 with CO_2 gas. ACS Omega 7 (1), 1395–1403. https://doi.org/10.1021/acsomega.1c06050.
Xu, C., Zhou, J., Xian, X., et al., 2024. Feasibility of the CO_2-ESGR technique for providing carbon-negative shale gas: A life cycle assessment. J. Clean. Prod. 484, 144353. https://doi.org/10.1016/j.jclepro.2024.144353.
Xu, H., Qin, Y., Yang, D., et al., 2024. Experimental investigation of gas diffusion kinetics and pore-structure characteristics during coalbed methane desorption within a coal seam. Gas Sci. Eng. 121, 205173. https://doi.org/10.1016/j.jgsce.2023.205173.
Yang, K., Conolly, P., Liu, L., et al., 2022. Quantitative characterization of methane adsorption in shale using low-field NMR. J. Nat. Gas Sci. Eng. 108, 104847. https://doi.org/10.1016/j.jngse.2022.104847.
Yao, Y., Liu, D., Xie, S., 2014. Quantitative characterization of methane adsorption on coal using a low-field NMR relaxation method. Int. J. Coal Geol. 131, 32–40. https://doi.org/10.1016/j.coal.2014.06.001.
Yao, Y., Liu, J., Liu, D., et al., 2019. A new application of NMR in characterization of multiphase methane and adsorption capacity of shale. Int. J. Coal Geol. 201, 76–85. https://doi.org/10.1016/j.coal.2018.11.018.

Yuan, J., Luo, D., Feng, L., 2015. A review of the technical and economic evaluation techniques for shale gas development. Appl. Energy 148, 49–65. https://doi.org/10.1016/j.apenergy.2015.03.040.
Yuan, S., Gang, H., Liu, Y., et al., 2023. Molecular interactions of CO_2 and CH_4 and their adsorption behaviour in kerogens with different grades of maturity. Mol. Simul. 49 (6), 536–550. https://doi.org/10.1080/08927022.2023.2176176.
Yuan, W., Pan, Z., Li, X., et al., 2014. Experimental study and modelling of methane adsorption and diffusion in shale. Fuel 117, 509–519. https://doi.org/10.1016/j.fuel.2013.09.046.
Zeraibi, A., Khan, A., 2024. Revolutionizing green energy: Natural gas, shale gas technology, and ecological footprint in the USA. Int. J. Green Energy 22 (10), 1899–1914. https://doi.org/10.1080/15435075.2024.2446982.
Zhang, B., Fu, X., Li, G., et al., 2020. An experimental study on the effect of nitrogen injection on the deformation of coal during methane desorption. J. Nat. Gas Sci. Eng. 83, 103529. https://doi.org/10.1016/j.jngse.2020.103529.
Zhang, C., Liu, S., Ma, Z., et al., 2021. Combined micro-proppant and supercritical carbon dioxide (SC-CO_2) fracturing in shale gas reservoirs: A review. Fuel 305, 121431. https://doi.org/10.1016/j.fuel.2021.121431.
Zhang, J., Shi, M., Wang, D., et al., 2022. Fields and directions for shale gas exploration in China. Nat. Gas. Ind. B 9 (1), 20–32. https://doi.org/10.1016/j.ngib.2021.08.014.
Zhang, N., Wang, X., Wang, S., et al., 2024. Multifractal characteristics on pore structure of Longmaxi shale using nuclear magnetic resonance (NMR). Geoenergy Sci. Eng. 241, 213176. https://doi.org/10.1016/j.geoen.2024.213176.
Zhao, G., Wang, C., 2019. Influence of CO_2 on the adsorption of CH_4 on shale using low-field nuclear magnetic resonance technique. Fuel 238, 51–58. https://doi.org/10.1016/j.fuel.2018.10.092.
Zheng, S., Yao, Y., Liu, D., et al., 2021. Quantitative characterization of multiphase methane in coals using the NMR relaxation method. J. Petrol. Sci. Eng. 198, 108148. https://doi.org/10.1016/j.petrol.2020.108148.
Zheng, S., Yao, Y., Sang, S., et al., 2022. Dynamic characterization of multiphase methane during CO_2-ECBM: An NMR relaxation method. Fuel 324, 124526. https://doi.org/10.1016/j.fuel.2022.124526.
Zhou, G., Hu, Z., Gu, Z., et al., 2021. Low-field NMR investigation of the dynamic adsorption−desorption process of shale gas. Energy & Fuels 35, 4762–4774. https://doi.org/10.1021/acs.energyfuels.0c01919.
Zhou, J., Liu, M., Xian, X., et al., 2019. Measurements and modelling of CH_4 and CO_2 adsorption behaviors on shales: Implication for CO_2 enhanced shale gas recovery. Fuel 251, 293–306. https://doi.org/10.1016/j.fuel.2019.04.041.
Zou, C., Dong, D., Wang, Y., et al., 2015. Shale gas in China: Characteristics, challenges and prospects (I). Petrol. Explor. Dev. 42 (6), 753–767. https://doi.org/10.1016/S1876-3804(15)30072-0.